Lee-Vortex Formation in Free-Slip Stratified Flow over Ridges. Part II: Mechanisms of Vorticity and PV Production in Nonlinear Viscous Wakes

C. C. EPIFANIO*

National Center for Atmospheric Research, Boulder, Colorado

D. R. DURRAN

Department of Atmospheric Sciences, University of Washington, Seattle, Washington

(Manuscript received 22 December 2000, in final form 17 August 2001)

ABSTRACT

The formation of orographic wakes and vortices is studied within the context of numerically simulated viscous flow with uniform basic-state wind and stability past elongated free-slip ridges. The viscosity and thermal diffusivity are sufficiently large that the onset of small-scale turbulence is suppressed. It is found in Part I of this study that wake formation in the viscous flow is closely tied to the dynamics of a low-level hydraulic-jump-like feature in the lee of the obstacle. Here the role of the hydraulic jump in producing the vorticity and potential vorticity (PV) of the viscous wake is considered.

A method for diagnosing vorticity production is developed based on a propagator analysis of the Lagrangian vorticity equation that generalizes Cauchy's formula for the evolution of vorticity in a Lagrangian framework. Application of the method reveals that the vertical vorticity of the wake originates through baroclinic generation and tilting in the mountain wave upstream of the jump. However, upstream of the jump the vertical vorticity is relatively weak. Vertical stretching in the jump then amplifies this vorticity significantly to produce the pronounced vertical vorticity anomalies along the shear lines at the lateral edges of the wake.

The PV of the wake is found to result mainly from thermal dissipation in the jump. In particular, thermal diffusion tends to diabatically modify the potential temperature field in the jump so as to create PV from the vertical vorticity already present. From the standpoint of PV conservation, the presence of both diabatic cooling (by thermal diffusion) and vertical vorticity at the base of the jump produces a vertical flux of PV through the lower boundary. The advective fluxes of PV along each side of the wake are then primarily balanced at steady state by fluxes of PV through the obstacle surface.

1. Introduction

As first shown by Smolarkiewicz and Rotunno (1989, hereafter SR89), numerical simulations of stratified flow past obstacles of sufficient height produce realistic wakes and vortices even when a free-slip condition is applied at the surface of the obstacle. The application of a free-slip condition precludes the formation of a viscous boundary layer at the obstacle surface; the vertical vorticity of the simulated wakes is thus clearly not due to boundary-layer separation. SR89 suggested that in free-slip flow the vertical vorticity of the wake instead derives from the baroclinic generation and tilting of vorticity in the gravity wave field produced by the obstacle. To illustrate their argument, SR89 considered a small-amplitude analysis of steady nondissipative flow with uniform basic-state buoyancy frequency N and flow speed u_0 past an obstacle of small nondimensional height $\epsilon = Nh_0/u_0$, where h_0 is the maximum height of the barrier. The authors showed that while the flow is free of vertical vorticity at $O(\epsilon)$, the linear [i.e., $O(\epsilon)$] mountain-wave solution (Smith 1980) implies the production of vertical vorticity at $O(\epsilon^2)$. In particular, $O(\epsilon^2)$ vertical vorticity is produced over the lee slope of the obstacle by tilting $O(\epsilon)$ baroclinically generated horizontal vorticity into the vertical through $O(\epsilon)$ vertical motions.

In Part I of this study (Epifanio and Durran 2002), we extended the small-amplitude theory of SR89 by explicitly computing the $O(\epsilon^2)$ flow fields using a weakly nonlinear semianalytic model. We considered flow over an elongated ridge-like obstacle in order to isolate the production of vertical vorticity at either end of the ridge. The weakly nonlinear solutions confirm the presence of $O(\epsilon^2)$ vertical vorticity anomalies over the ends of the ridge as predicted by SR89 (see also Rotunno et

*Current affiliation: Department of Atmospheric Sciences, Texas A&M University, College Station, Texas.

Corresponding author address: Craig C. Epifanio, Department of Atmospheric Sciences, Texas A&M University, 3150 TAMU, College Station, TX 77843-3150.
E-mail: cepi@ariel.met.tamu.edu

© 2002 American Meteorological Society

al. 1999). Nonetheless, the $O(\epsilon^2)$ velocity fields (which are not uniquely determined by the vertical vorticity) were found to be inconsistent with the flow fields observed in developing vortices in previous nonlinear numerical experiments (e.g., Rotunno and Smolarkiewicz 1991; Schär and Durran 1997). On the basis of the $O(\epsilon^2)$ results, Part I concluded that the mechanism of vorticity tilting in nondissipative flow as described by weakly nonlinear theory cannot by itself account for lee-vortex formation. Additional finite-amplitude and/or dissipative effects must thus play a role in the production of the simulated vortices.

Part I extended this analysis by considering fully nonlinear numerical simulations of wake formation in stratified viscous flow past free-slip ridges of moderate height ($\epsilon \leq 2.2$). The most significant discrepancy between the numerically simulated flows and the weakly nonlinear results was the presence of a low-level hydraulic-jump-like feature downstream of the obstacle in the fully nonlinear viscous case. In many respects the wake produced in the nonlinear numerical simulations resembled that produced in the shallow-water calculations of Schär and Smith (1993, hereafter SS93), with flow reversal behind the jump and narrow bands of vertical vorticity extending downstream from the lateral ends of the jump. In conventional shallow-water theory, vertical vorticity production occurs solely within the hydraulic jump and the mechanisms of vorticity generation are therefore left unspecified. Similarly, the pronounced vorticity anomalies downstream of the jump in the stratified viscous case strongly suggest the creation of vertical vorticity in the jump, but the mechanism of vorticity production could not be diagnosed from the qualitative analysis in Part I.

The production of vorticity and potential vorticity (PV) in shallow-water hydraulic jumps was first explored in detail by Pratt (1983). Pratt showed that PV production in a steady two-dimensional jump is related to spatial gradients in the Bernoulli deficit ΔB caused by the jump. This interesting result was generalized by SS93 to show that for steady shallow-water flow the Bernoulli function serves as the effective streamfunction for the flux of PV. The corresponding result for steady stratified flow relates the flux of PV to the gradient of the Bernoulli function on an isentrope (Schär 1993). Schär and Durran (1997, hereafter SD97) have explored the creation of Bernoulli gradients and the associated PV fluxes in stratified flow past an isolated obstacle. Their analysis is similar to the shallow-water approach in that the detailed mechanisms of vorticity and PV generation are left unspecified. Note that while SD97 consider the effects of wave breaking in PV generation, they do not explicitly consider the role of low-level analogues to hydraulic jumps.

A recent study by Rotunno et al. (1999, hereafter RGS99) extends the small-amplitude theory of SR89 by considering steady inviscid flow with thermal Rayleigh damping over a small isolated obstacle. The introduction of thermal dissipation acts to extend the baroclinically generated vertical vorticity of the wave field downwind in a pair of PV streamers. Numerical simulations of viscous flow with uniform viscosity and thermal diffusivity past a large free-slip obstacle produced wake features qualitatively similar to those found in the small-amplitude calculations. The RGS99 study shows that even in dissipative flow with significant PV generation and associated Bernoulli gradients, the vertical vorticity of the wake may originate through baroclinic generation and tilting. However, in their analysis of the numerical results RGS99 relied mainly on inferences drawn from the small-amplitude theory; fully nonlinear effects were thus, in large part, left unexplored.

The purpose of the present study is to analyze in detail the mechanisms of vorticity and PV generation in free-slip, nonlinear viscous wakes such as those simulated in Part I. Particular attention is given to fully nonlinear effects and to the role of the hydraulic jump in producing vorticity and PV. We consider viscous and thermally conducting flow of sufficiently low Reynolds number that the onset of small-scale turbulence is suppressed. As discussed in Part I, consideration of the laminar viscous model simplifies the analysis of vorticity and PV generation relative to nominally inviscid simulations in which the effects of subgrid-scale motions must be parameterized. Nonetheless, as will be discussed in section 6, the structure and evolution of the wakes in the nonlinear viscous flow are qualitatively similar to that obtained in otherwise identical inviscid simulations with parameterized subgrid-scale turbulence.

The following section briefly reviews the experimental setup considered in Part I. In section 3 we develop a new method for diagnosing vorticity production based on a propagator analysis of the Lagrangian vorticity equation. The method involves decomposing the total vorticity field into parts, each of which is associated in a Lagrangian sense with vorticity generation in a particular region of the flow or by a particular generation mechanism. Section 4 employs the decomposition method to show that in the nonlinear viscous simulations the vertical vorticity of the wake does in fact originate through the baroclinic generation and tilting mechanism proposed by SR89. However, the hydraulic jump plays a crucial role by subsequently amplifying the vorticity several-fold through stretching, thereby producing the pronounced vertical vorticity anomalies that define the edges of the wake. Section 5 shows that dissipation in the jump is primarily responsible for PV generation in the flow, and the mechanisms of PV generation are discussed in some detail. It is shown that from the standpoint of quasi-steady PV conservation, the downstream advection of PV in the wake is balanced primarily by fluxes of PV through the obstacle surface. The final section contains conclusions.

2. Experimental setup and background

Details of the experimental setup and numerical simulations considered in the present study are as given in

section 2 of Part I. Here we briefly describe the physical and mathematical framework of the experiments to establish notation and cite a few basic results for later reference.

a. Physical framework

We consider nonrotating, compressible Boussinesq flow as described by

$$\frac{\partial u_i}{\partial t} + u_j\frac{\partial u_i}{\partial x_j} + \frac{\partial P}{\partial x_i} - \delta_{i3}b = -\frac{\partial T_{ij}}{\partial x_j}, \tag{1}$$

$$\frac{\partial b}{\partial t} + u_j\frac{\partial b}{\partial x_j} + N^2 w = -\frac{\partial B_j}{\partial x_j}, \quad \text{and} \tag{2}$$

$$\frac{\partial P}{\partial t} + c_s^2\frac{\partial u_j}{\partial x_j} = 0, \tag{3}$$

where $\mathbf{x} = (x_1, x_2, x_3) = (x, y, z)$ is the spatial position vector; $\mathbf{u} = (u, v, w)$ is the fluid velocity; P is the Boussinesq disturbance pressure and b the buoyancy; N is the basic-state buoyancy frequency; and c_s is the constant Boussinesq sound speed. The flow is assumed viscous and thermally conducting. The viscous stress and diffusive heat flux are then given by

$$T_{ij} = -K_M\left(\frac{\partial u_i}{\partial x_j} + \frac{\partial u_j}{\partial x_i} - \frac{2}{3}\delta_{ij}\frac{\partial u_k}{\partial x_k}\right), \quad \text{and} \tag{4}$$

$$B_j = -K_H\frac{\partial b}{\partial x_j}, \tag{5}$$

where the kinematic viscosity K_M and the thermal diffusivity K_H are constants. The Prandtl number $\mathrm{Pr} = K_M/K_H$ is unity. Approximate free-slip and thermal insulation conditions are adopted at the lower boundary for T_{ij} and B_j, respectively (see Part I). We consider disturbances to a basic state with constant N and uniform basic velocity $\mathbf{u}_0 = (u_0, 0, 0)$. Basic-state pressure and potential temperature variables may then be defined as

$$b_0(z) = -g + N^2 z, \qquad P_0(z) = P_s - gz + \frac{1}{2}N^2 z^2, \tag{6}$$

where P_s is the constant reference surface pressure for the Boussinesq system.

We define the topography to be a smooth three-dimensional ridge with long axis normal to the incident wind. The specific ridge shape is given by (6) and (7) of Part I with the relevant parameters being the maximum barrier height h_0, the streamwise length scale a, and the horizontal aspect ratio (ratio of cross-stream to streamwise length scales) β. In the present simulations the nondimensional ridge height is set at $\epsilon = Nh_0/u_0 = 1.8$ and the horizontal aspect ratio is $\beta = 3$. The Reynolds number of the flow is given by $\mathrm{Re} = u_0 h_0/K_M = 120$. The remaining flow parameters are as specified in Part I.

In addition to the terms in the physical equations of motion (1)–(3), the numerical model also includes weak numerical filter terms of the form

$$-\alpha\left(\left.\frac{\partial^4 u_i}{\partial x^4}\right|_\gamma + \left.\frac{\partial^4 u_i}{\partial y^4}\right|_\gamma\right), \qquad -\alpha\left(\left.\frac{\partial^4 b}{\partial x^4}\right|_\gamma + \left.\frac{\partial^4 b}{\partial y^4}\right|_\gamma\right), \tag{7}$$

where γ is the terrain-following computational coordinate defined by (21) of Part I and where the derivatives are computed at constant γ. As discussed in Part I and in section 5 below, the filter terms are dominated by the physical viscosity and thermal diffusion at all scales of interest in the simulated flow. The filters thus play a negligible role in the dynamics of the flow.

b. Basic considerations

Under the assumption of incompressible flow, the curl of (1) yields the vorticity equation

$$\frac{\partial \boldsymbol{\zeta}}{\partial t} + (\mathbf{u}\cdot\nabla)\boldsymbol{\zeta} = (\boldsymbol{\zeta}\cdot\nabla)\mathbf{u} - \mathbf{k}\times\nabla b + \nabla\times\mathbf{F}, \tag{8}$$

where $\boldsymbol{\zeta} = (\xi, \eta, \zeta)$ is the vorticity, $\mathbf{k}$ the vertical unit vector, and where for notational convenience we define $F_i = -\partial T_{ij}/\partial x_j$. In the Boussinesq system the baroclinicity vector $-\mathbf{k}\times\nabla b$ is horizontal and parallel to contours of $b + b_0$. For constant kinematic viscosity the dissipative term takes the form

$$\nabla\times\mathbf{F} = K_M\nabla^2\boldsymbol{\zeta},$$

in which case viscous effects diffuse vorticity but do not directly create vorticity. However, if K_M varies in space as in the case of an eddy viscosity, then vorticity may be directly forced by the $\nabla\times\mathbf{F}$ term.

The PV equation formed from (8) and (2) is

$$\frac{\partial Q}{\partial t} + (\mathbf{u}\cdot\nabla)Q = \nabla(b + b_0)\cdot(\nabla\times\mathbf{F}) + \boldsymbol{\zeta}\cdot\nabla H, \tag{9}$$

where $H = -\partial B_j/\partial x_j$ and where the PV is defined as

$$Q = \boldsymbol{\zeta}\cdot\nabla(b + b_0). \tag{10}$$

Equation (9) is often usefully considered in the equivalent conservation form

$$\frac{\partial Q}{\partial t} + \nabla\cdot\mathbf{J} = 0, \tag{11}$$

where

$$\mathbf{J} = \mathbf{u}Q + \nabla(b + b_0)\times\mathbf{F} - \boldsymbol{\zeta}H \tag{12}$$

is the total flux of PV. As shown by Schär (1993, hereafter S93), the PV flux (12) may be expressed entirely in terms of flow variables as (in the present Boussinesq case)

$$\mathbf{J} = \nabla(b + b_0)\times\left(\frac{\partial\mathbf{u}}{\partial t} + \nabla R\right) - \boldsymbol{\zeta}\frac{\partial b}{\partial t}, \tag{13}$$

where R is the Boussinesq Bernoulli function

$$R = \frac{1}{2}\mathbf{u}\cdot\mathbf{u} + P + P_0 - (b + b_0)z. \tag{14}$$

At steady state the flux of PV is parallel to the intersections of surfaces of constant R and $b + b_0$.

3. Lagrangian vorticity decompositions: Theory and implementation

Here we develop a new method for diagnosing vorticity dynamics in numerically simulated flows. The method involves decomposing the vorticity vector into parts, each of which is associated with vorticity generation during a specific time interval along a particle trajectory. The method also provides a means for identifying the part of the vorticity due to generation by a particular part of the vorticity source (e.g., baroclinic generation). The physical interpretation of the method is most readily established in a Lagrangian context, and sections 3a–3c develop the relevant theory in terms of a propagator (or Green's function) analysis of the Lagrangian vorticity equation. While the Lagrangian analysis provides a physical basis for the method, the actual decompositions are computed in an Eulerian framework in the numerical model. The implementation of the method is described in section 3d.

a. The propagator framework

We first rewrite the vorticity equation (8) in the Lagrangian form

$$\frac{d\zeta_i}{dt} = \frac{\partial u_i}{\partial x_j}\zeta_j + g_i, \tag{15}$$

where the source term $\mathbf{g}$ includes baroclinic and viscous parts and d/dt denotes the Lagrangian (or material) derivative. For the purposes of the present analysis we take both $\mathbf{u}$ and $\mathbf{g}$ to be specified functions of $(\mathbf{x}, t)$ (e.g., as given by numerical simulation). Then following a given particle trajectory, (15) can be regarded as a system of linear ordinary differential equations in time. We thus seek to integrate

$$\frac{d\zeta_i}{dt} = M_{ij}(t)\zeta_j + g_i(t), \qquad \zeta_i(t_0) = \zeta_{0i}, \tag{16}$$

where $M_{ij} = \partial u_i/\partial x_j$ is the relative motion tensor and ζ_{0i} is the ith component of the initial vector $\boldsymbol{\zeta}_0$.

Solutions to (16) can be obtained in terms of a propagator matrix $\mathbf{P}(t, \tau)$ satisfying

$$\frac{dP_{ij}}{dt}(t, \tau) = M_{ik}(t)P_{kj}(t, \tau) + \delta(t - \tau)\delta_{ij}, \quad \text{and} \tag{17a}$$

$$P_{ij}(t, \tau) = 0 \quad \text{for } t < \tau, \tag{17b}$$

where δ is the Dirac delta function and δ_{ij} is the Kronecker delta.[1] Note that the jth column of $\mathbf{P}$ is the response to a unit impulse of vorticity applied along the jth coordinate direction at time τ. Given $\mathbf{P}$, the solution to (16) for $t > t_0$ takes the form

$$\zeta_i(t) = P_{ij}(t, t_0)\zeta_j(t_0) + \int_{t_0}^{t} P_{ij}(t, \tau)g_j(\tau)\, d\tau. \tag{18}$$

The propagator matrix satisfying (17) is most easily derived in a Lagrangian formulation (e.g., Dutton 1976, section 5.7). Define the Lagrangian coordinate $\mathbf{X}(\mathbf{x}, t)$ to be the spatial position at time t_0 of the particle at $(\mathbf{x}, t)$. The inverse $\mathbf{x}(\mathbf{X}, t)$ gives the trajectory of the particle with Lagrangian coordinate $\mathbf{X}$. Note that we may consider a given field ψ to be a function of $(\mathbf{x}, t)$ or $(\mathbf{X}, t)$. The material time derivative may thus be written

$$\frac{d\psi}{dt} = \frac{\partial \psi}{\partial t_X}, \tag{19}$$

where $\partial/\partial t_X$ denotes a time derivative with $\mathbf{X}$ held fixed (i.e., following a particle trajectory). With these definitions, the derivation in appendix A shows that the solution to (17) takes the form

$$P_{ij}(t, \tau) = \frac{\partial x_i}{\partial X_k}(t)\frac{\partial X_k}{\partial x_j}(\tau), \tag{20}$$

where the derivatives are evaluated at times t and τ along the particle trajectory.

b. Physical interpretation as an extension of Cauchy's formula to stratified and viscous flow

The physical significance of the propagator matrix (20) is most clearly revealed by considering the action of the matrix on an arbitrary material line element at time τ. To be concrete, let $\delta\mathbf{x}(t)$ be a material line element anchored on the particle at Lagrangian coordinate $\mathbf{X}$; that is, $\delta\mathbf{x}(t) = \mathbf{x}(\mathbf{X}', t) - \mathbf{x}(\mathbf{X}, t)$, where $\mathbf{X}$ and $\mathbf{X}'$ are fixed and $\delta\mathbf{X} = \mathbf{X}' - \mathbf{X}$ is supposed infinitesimal. We then have

$$P_{ij}(t, \tau)\delta x_j(\tau) = \frac{\partial x_i}{\partial X_k}(t)\frac{\partial X_k}{\partial x_j}(\tau)\frac{\partial x_j}{\partial X_r}(\tau)\delta X_r = \frac{\partial x_i}{\partial X_k}(t)\delta X_k$$
$$= \delta x_i(t),$$

where all derivatives are evaluated for the particle at $\mathbf{X}$. In matrix notation this is

$$\mathbf{P}(t, \tau)\delta\mathbf{x}(\tau) = \delta\mathbf{x}(t), \tag{21}$$

showing that $\mathbf{P}(t, \tau)$, acting on the material line element $\delta\mathbf{x}$ at time τ, returns the same material line element at the later time t. *The propagator thus accounts for the stretching and tilting of the element by the flow field over the time interval from τ to t.*

Combining (18) and (20) we find that the vorticity of a given fluid particle is described in a Lagrangian sense by

[1] Solutions to linear systems of the form (16) are often alternatively expressed in terms of the so-called fundamental matrix solutions of the system (e.g., Coddington and Levinson 1955, sections 3.2 and 3.3). See Grimshaw (1993, section 2.3) and appendix A for the relationship between the fundamental matrix approach and the propagator formalism adopted here.

$$\zeta_i(t) = \frac{\partial x_i}{\partial X_j}(t)\zeta_j(t_0) + \int_{t_0}^{t} \frac{\partial x_i}{\partial X_k}(t)\frac{\partial X_k}{\partial x_j}(\tau)g_j(\tau)\, d\tau, \quad (22)$$

where we have used $\partial X_k/\partial x_j(t_0) = \delta_{jk}$. The first term on the right-hand side of (22) expresses the fact that for $\mathbf{g} = 0$ the vorticity vectors described by (15) behave like material line elements. This term describes the stretching and tilting of the initial vorticity $\boldsymbol{\zeta}_0$ over the time interval from t_0 to t and is equivalent to the incompressible form of Cauchy's formula for the vorticity in inviscid and barotropic flow (e.g., Serrin 1959; Dutton 1976, section 10.11.3). The term involving the vorticity source $\mathbf{g}$ represents an extension of the Cauchy result to include baroclinic and viscous vorticity generation. The integrand in (22) describes the stretching and tilting over the time interval from τ to t of the vorticity $\mathbf{g}(\tau)d\tau$ generated during the increment from τ to $\tau + d\tau$.

In the discussion above, all quantities are evaluated following a given fluid particle (i.e., at fixed $\mathbf{X}$) and the spatial arguments have thus been dropped for convenience. However, all quantities depend on $\mathbf{X}$ and for clarity we show the $\mathbf{X}$ dependence explicitly in the following.

c. Vorticity decompositions

The propagator formalism provides a natural means of decomposing the vorticity vector into parts that are associated with vorticity generation during specific time intervals along a particle trajectory. In the present context, suppose that the particle at $\mathbf{X}$ spends the time interval from t_0 to $c(\mathbf{X})$ upstream of the hydraulic jump and the interval from $c(\mathbf{X})$ to t in and downstream of the jump. Given $\boldsymbol{\zeta}_0 = 0$, (22) may then be decomposed as $\boldsymbol{\zeta} = \boldsymbol{\zeta}^W + \boldsymbol{\zeta}^J$, where

$$\zeta_i^W(\mathbf{X}, t) = \int_{t_0}^{c(\mathbf{X})} \frac{\partial x_i}{\partial X_k}(\mathbf{X}, t)\frac{\partial X_k}{\partial x_j}(\mathbf{X}, \tau)g_j(\mathbf{X}, \tau)\, d\tau, \quad (23a)$$

and

$$\zeta_i^J(\mathbf{X}, t) = \int_{c(\mathbf{X})}^{t} \frac{\partial x_i}{\partial X_k}(\mathbf{X}, t)\frac{\partial X_k}{\partial x_j}(\mathbf{X}, \tau)g_j(\mathbf{X}, \tau)\, d\tau. \quad (23b)$$

The integral in (23a) may be interpreted as the part of the total vorticity vector at time t due to vorticity generated upstream of the jump and subsequently stretched and tilted from its time of generation to time t. The second integral is then the part due to vorticity generated in and downstream of the jump and subsequent stretching and tilting of that vorticity through time t.

The propagator analysis also allows the vorticity vector to be decomposed into parts that are associated with particular parts of the vorticity source. For example, suppose we write the vorticity source as $\mathbf{g} = \mathbf{g}^B + \mathbf{g}^V$, where $\mathbf{g}^B$ denotes the generation of vorticity by baroclinicity and $\mathbf{g}^V$ represents viscous (or eddy viscous) effects. The integral term in (22) can then be separated into two separate integrals, one involving $\mathbf{g}^B$ and the other $\mathbf{g}^V$. The integral involving $\mathbf{g}^B$ may be interpreted as the part of the vorticity vector due to baroclinic generation and subsequent stretching and tilting. The integral with $\mathbf{g}^V$ is then the part of the vorticity vector originating in viscous effects.

More generally, suppose we expand the source function $\mathbf{g}$ into a sum of arbitrarily defined partial sources as

$$g_i = g_i^A + g_i^B + \cdots = \sum_\nu g_i^\nu. \quad (24a)$$

Substituting into (22) we find

$$\zeta_i = \zeta_i^0 + \zeta_i^A + \zeta_i^B + \cdots = \zeta_i^0 + \sum_\nu \zeta_i^\nu, \quad (24b)$$

where

$$\zeta_i^0(\mathbf{X}, t) = \frac{\partial x_i}{\partial X_j}(\mathbf{X}, t)\zeta_j(\mathbf{X}, t_0), \quad \text{and} \quad (24c)$$

$$\zeta_i^\nu(\mathbf{X}, t) = \int_{t_0}^{t} \frac{\partial x_i}{\partial X_k}(\mathbf{X}, t)\frac{\partial X_k}{\partial x_j}(\mathbf{X}, \tau)g_j^\nu(\mathbf{X}, \tau)\, d\tau. \quad (24d)$$

Note that the vorticity expansion defined by (24) is broad enough to encompass spatial and temporal decompositions such as that described by (23). [Specifically, setting $\mathbf{g}^W = \mathbf{g}$ upstream of the jump and $\mathbf{g}^W = 0$ in and downstream of the jump reproduces (23a) upon substitution into (24d).] We thus adopt the form (24) for the decompositions discussed below.

d. Implementation and boundary conditions

With $\mathbf{u}$ specified as before, the solution to

$$\frac{d\zeta_i^0}{dt} = M_{ij}\zeta_j^0 = \frac{\partial u_i}{\partial x_j}\zeta_j^0, \quad \text{and} \quad (25a)$$

$$\zeta_i^0(\mathbf{X}, t_0) = \zeta_i(\mathbf{X}, t_0) = \zeta_{0i}(\mathbf{x}) \quad (25b)$$

is (24c). Similarly, (24d) solves

$$\frac{d\zeta_i^\nu}{dt} = \frac{\partial u_i}{\partial x_j}\zeta_j^\nu + g_i^\nu, \quad \text{and} \quad (26a)$$

$$\zeta_i^\nu(\mathbf{X}, t_0) = 0. \quad (26b)$$

The vorticity decomposition (24) can thus be obtained by numerically integrating (25) and (26) with the specified $\mathbf{u}$ and for each specified $\mathbf{g}^\nu$. In the present work we need only consider (26) since $\boldsymbol{\zeta}_0 = 0$. The integration of (26) is implemented by adding the Eulerian form of (26a) to the set of equations solved by the numerical model so that (26a) is integrated simultaneously with (1)–(3). The flow field $\mathbf{u}(\mathbf{x}, t)$ and the partial source $\mathbf{g}^\nu(\mathbf{x}, t)$ are then determined by the numerical solutions to (1)–(3).[2] Details of the numerical implementation are included in appendix B. Note that since (26a) is integrated in Eulerian form, we obtain the partial vorticity

[2] Note that the Eqs. (26) are decoupled from the equations of motion (1)–(3) in the sense that the vorticity computed from (26) does not feed back on $\mathbf{u}$, b, and P.

(24d) as a function of ($\mathbf{x}$, t) rather than ($\mathbf{X}$, t). That is, $\boldsymbol{\zeta}^\nu$ is obtained for all fluid particles at a fixed time rather than as a function of time following a single trajectory.

Integration of the vorticity equation typically requires the specification of boundary conditions for $\boldsymbol{\zeta}$ at the interface of fluid and obstacle (see, e.g., Morton 1984). However, (15) shows that the vorticity of a particle in the fluid interior is completely determined by giving the initial vorticity of the particle and specifying $\mathbf{u}$ and $\mathbf{g}$ along the particle trajectory. Since fluid particles do not cross the obstacle surface (i.e., the flow at the surface is tangent to the surface), a particle in the interior of the flow becomes aware of boundary information only through $\mathbf{u}$ and $\mathbf{g}$. In the present context both $\mathbf{u}$ and $\mathbf{g}$ are specified and we need not explicitly consider boundary conditions at the obstacle surface to determine $\boldsymbol{\zeta}$. Equation (26a) is thus implemented numerically without reference to $\boldsymbol{\zeta}(x, y, h, t)$.

As in the integrations of (1) and (2), weak numerical filters analogous to (7) are added to (26a) to maintain numerical stability. For $\boldsymbol{\zeta}^\nu = \boldsymbol{\zeta}$, these terms closely approximate the (Cartesian) curl of the first of (7). The dissipative vorticity source associated with the curl of the filter terms in the momentum equations is then omitted from the source function $\mathbf{g}$ for consistency. As such, the present calculations do not address the effect of the filters on the vorticity field. However, as discussed in section 2 of Part I and in section 5 below, physical viscosity and thermal diffusion dominate numerical filtering in the present calculations so that the influence of the filter terms is small.

Finally, let $\boldsymbol{\zeta}^g$ be the result of integrating (26) with the full vorticity source $\mathbf{g}$ included in place of the partial source $\mathbf{g}^\nu$. In principle, with $\boldsymbol{\zeta}_0 = 0$ we should have $\boldsymbol{\zeta}^g = \boldsymbol{\zeta}$ [cf. (22)]. In practice, $\boldsymbol{\zeta}^g$ will not exactly equal $\boldsymbol{\zeta} = \boldsymbol{\nabla} \times \mathbf{u}$ (computed in terms of derivatives of the flow) due to discretization errors in the implementation of (1)–(3) and (26a). The fidelity of the vorticity integrations must therefore be verified by comparing the integrated vorticity $\boldsymbol{\zeta}^g$ with the discretized curl of the flow field. Having verified the integrations, suppose we then expand the vorticity source as in (24a) and integrate (26) with each $\mathbf{g}^\nu$ to obtain the partial vorticities $\boldsymbol{\zeta}^\nu$. By the linearity of the finite-difference approximation to (26) we necessarily have $\boldsymbol{\zeta}^g = \Sigma_\nu \boldsymbol{\zeta}^\nu$.

4. Nonlinear vorticity production in viscous lee-vortex flows

In this section we apply the Lagrangian vorticity decomposition method of the previous section to viscous simulations similar to that described in Part I, which considered flow with Reynolds number Re = 120 over a ridge of height $\epsilon = 1.8$ and aspect ratio $\beta = 5$. In the present simulations the ridge is shortened so that $\beta = 3$ and the model domain is correspondingly reduced to decrease the computational burden. The remaining parameters (physical and numerical) are identical to those used in Part I. As in Part I, horizontal plots show fields on the terrain-following coordinate surface $N\gamma/u_0 = 0.351 \approx \pi/9$, which is the fourth scalar grid level from the lower boundary. All plots in this section and in section 5a are for the first time at which leeside flow stagnation occurs along the line of symmetry on the terrain-following analysis surface, which in this case is $u_0t/a = 3$.

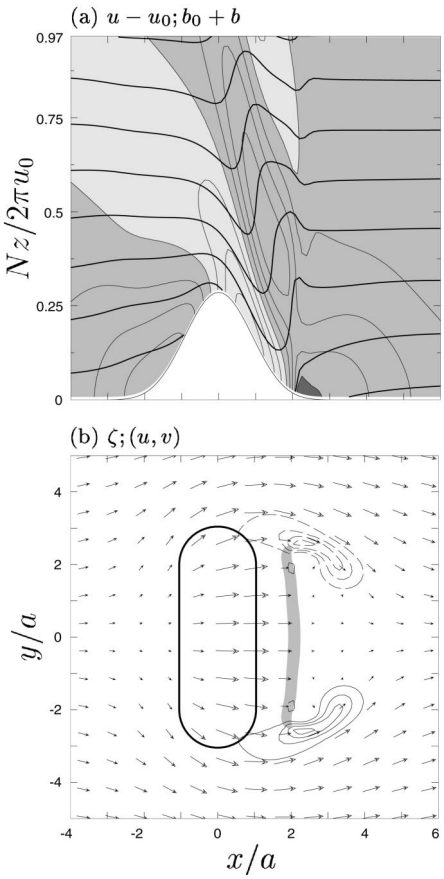

FIG. 1. Nonlinear numerical simulation of free-slip viscous flow with Re = 120 over an isolated ridge with $\beta = 3$ and $\epsilon = 1.8$. Fields in (a) are shown in the plane of symmetry $y = 0$; (b) shows fields on the terrain-following coordinate surface $N\gamma/u_0 \approx \pi/9$. Heavy solid line in (b) is the topographic contour at half maximum height. All fields are shown at time $u_0t/a = 3$. (a) Potential temperature $(b + b_0)/Nu_0$ (dark lines; contour interval is 0.833) and disturbance speed $(u - u_0)/\epsilon u_0$ [contour interval is 0.139, light shading is positive, dark shading is negative; values less than $-1/\epsilon$ (i.e., reversed flow) indicated by darkest shading]; (b) $\zeta/\epsilon^2\delta N$ (contour interval is 0.21, solid line is positive and dashed line is negative) and $(u, v)/u_0$ (maximum vector length is 1.625). Shading in (b) indicates the hydraulic jump region as defined by values of $(a/\epsilon N u_0)\partial b/\partial x$ less than -0.579.

Figure 1 shows the basic structure of the wake in the $\beta = 3$ case. Comparison with Figs. 3a and 4f of Part I suggests that the wake is similar in structure to the $\beta = 5$ case discussed therein. Above the lee slope the low-level isentropes in Fig. 1a are strongly depressed and the flow is accelerated. Downstream the isentropes abruptly return to nearly their upstream heights in a structure resembling a hydraulic jump. Behind the jump

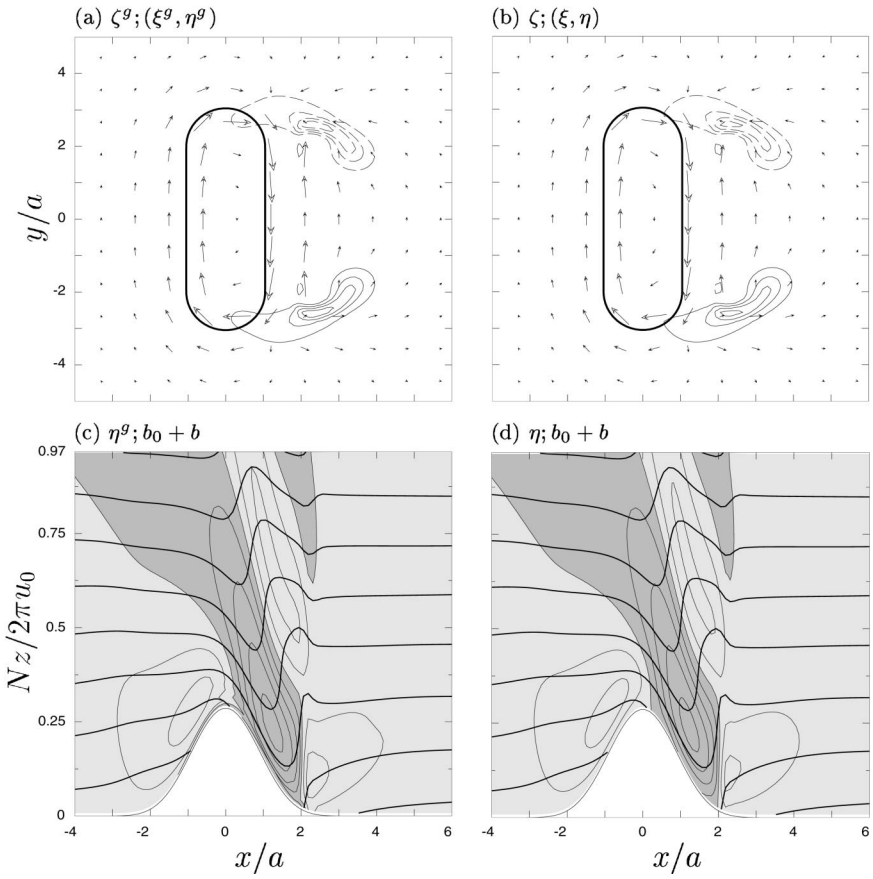

FIG. 2. Verification of partial vorticity integrations: (a) and (b) fields on the terrain-following coordinate surface $N\gamma/u_0 \approx \pi/9$; (c) and (d) the plane of symmetry $y = 0$. All fields are shown at time $u_0t/a = 3$. (a) Integrated vertical vorticity $\zeta^g/\epsilon^2\delta N$ (contour interval is 0.21) and integrated horizontal vorticity $(\xi^g, \eta^g)/\epsilon N$ (maximum vector length is 0.46); (b) vertical vorticity $\zeta/\epsilon^2\delta N$ and horizontal vorticity $(\xi, \eta)/\epsilon N$ as given by the curl of the velocity field; (c) integrated cross-stream vorticity $\eta^g/\epsilon N$ (contour interval is 0.15) and potential temperature $(b_0 + b)/Nu_0$ (contour interval is 0.833); (d) cross-stream vorticity $\eta/\epsilon N$.

the flow is decelerated and the cross-stream vorticity $\eta \approx \partial u/\partial z$ is positive. In plan view the lee-slope flow is accelerated upstream of the jump (as defined by the shaded area of strongly negative $\partial b/\partial x$ in Fig. 1b) while a wake of nearly stagnant fluid is seen behind the jump. Concentrated anomalies of vertical vorticity extend downstream from the lateral ends of the jump and mark the shearlines along the lateral edges of the wake. Further discussion of the wake structure is given in Part I.

We now apply the vorticity decomposition method to the flow in Fig. 1 to diagnose the mechanisms of vorticity production. As discussed in section 3d, the accuracy of the method must first be established by comparing $\boldsymbol{\zeta} = \boldsymbol{\nabla} \times \mathbf{u}$ with the result $\boldsymbol{\zeta}^g$ obtained by integrating the vorticity equation (26) with the full vorticity source $\mathbf{g}$. Figure 2a shows the integrated vertical vorticity component ζ^g and horizontal vorticity vector (ξ^g, η^g) at time $u_0t/a = 3$. Comparison with Fig. 2b suggests that the integrated vorticity $\boldsymbol{\zeta}^g$ accurately reproduces $\boldsymbol{\zeta}$ at this time. Similarly, comparison of Figs. 2c and 2d reveals excellent agreement between η^g and η along the centerline except perhaps at the lower boundary.[3] Even at the lower boundary the agreement is sufficient for the present discussion.

Figure 3 shows a series of calculations addressing the mechanisms of vertical vorticity production in the viscous wake flow. The pronounced maxima in $|\zeta|$ downstream of the ends of the jump in Fig. 1b suggest that the flow in the jump in some way contributes to the

[3] The discrepancy between η^g and η near the surface is due partly to the use of one-sided vertical derivatives in the computation of $\mathbf{g}$ at the lower boundary and partly to discretization errors in the advection and stretching/tilting terms of (1) and (26a). The latter errors could likely be reduced by formulating the advection and stretching/tilting terms in (26a) in a way that is consistent with the discretized curl of the discretized version of (1). We do not pursue this approach here and instead discretize (26a) directly without consideration of the curl of (1) (see appendix B). Greater consistency in the numerical approximations to (1)–(3) and (26a) would be required for time integrations longer than those considered here.

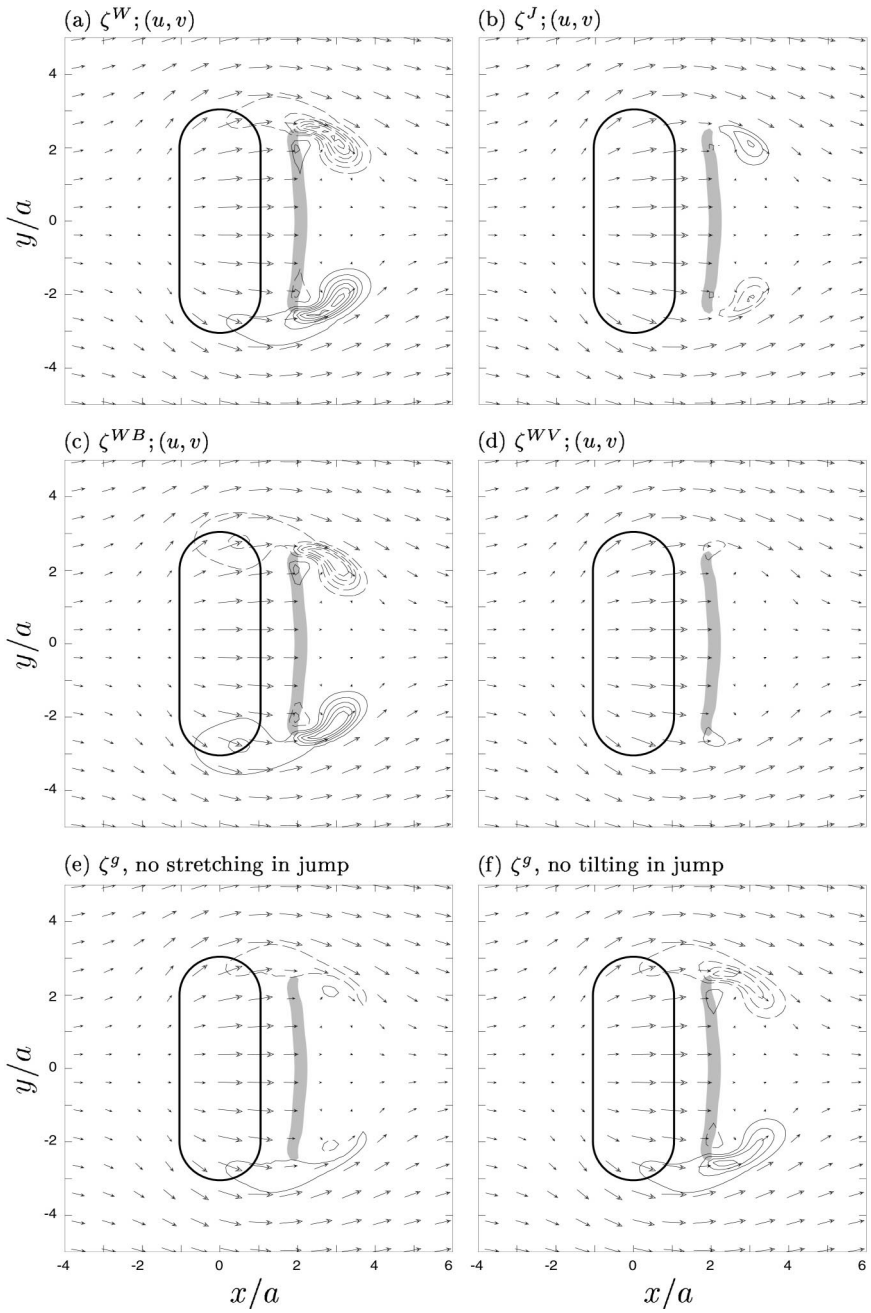

FIG. 3. Mechanisms of vertical vorticity production as diagnosed from Lagrangian vorticity decompositions. All fields are shown on the low-level analysis surface $N\gamma/u_0 \approx \pi/9$ at time $u_0t/a = 3$. Shading and vectors in all panels are as in Fig. 1b. (a) and (b) Decomposition of vorticity according to generation upstream of the jump (wave vorticity) and generation in or downstream of the jump (jump vorticity): (a) vertical component of wave vorticity $\zeta^W/\epsilon^2\delta N$ (contour interval is 0.21); (b) vertical component of jump vorticity $\zeta^J/\epsilon^2\delta N$. (c) and (d) Further decomposition of wave vorticity $\boldsymbol{\zeta}^W$ according to baroclinic and viscous sources: (c) vertical component of baroclinic part of wave vorticity $\zeta^{WB}/\epsilon^2\delta N$; (d) vertical component of viscous part of wave vorticity $\zeta^{WV}/\epsilon^2\delta N$. (e) and (f) Vertical component of vorticity computed using full vorticity source **g** as in Fig. 2a, except (e) without stretching of vertical vorticity in the jump and (f) without vertical tilting of horizontal vorticity in the jump.

production of vertical vorticity in the wake. However, it is not clear whether the maxima in $|\zeta|$ are due to vorticity generation in the jump or whether the flow in the jump instead modifies vorticity generated upstream. To address the importance of vorticity generation in the jump, let V^J be the volume of fluid in and downstream of the jump as given by (cf. Fig. 4e of Part I),

$$V^J = \left\{(x, y, z, t) \,|\, x \geq 0,\ z \geq h,\ \frac{\partial b}{\partial x}(x, y, z, t) < 0\right\}$$

and decompose the vorticity source $\mathbf{g}$ as

$$\mathbf{g} = \mathbf{g}^W + \mathbf{g}^J,$$

where

$$\mathbf{g}^J = \begin{cases} \mathbf{g} = -\mathbf{k} \times \nabla b + \nabla \times \mathbf{F}, & \text{if } (\mathbf{x}, t) \in V^J \\ 0, & \text{otherwise.} \end{cases}$$

At low levels $\mathbf{g}^J$ describes the generation of vorticity in and downstream of the jump while $\mathbf{g}^W$ represents generation in the mountain wave upstream of the jump. The vertical components of the partial vorticities $\boldsymbol{\zeta}^W$ and $\boldsymbol{\zeta}^J$ generated by each partial source are shown in Figs. 3a and 3b. Comparison of these figures reveals that the vertical vorticity in the wake originates almost entirely through vorticity generation upstream of the jump. In fact, the vorticity generated in and downstream of the jump contributes in a contrary sense to the net vertical vorticity of the wake.

To examine the mechanism by which $\boldsymbol{\zeta}^W$ is generated, the vorticity source upstream of the jump may be further decomposed into baroclinic and viscous parts. Let

$$\mathbf{g}^W = \mathbf{g}^{WB} + \mathbf{g}^{WV},$$

where the baroclinic part of $\mathbf{g}^W$ is defined as

$$\mathbf{g}^{WB} = \begin{cases} -\mathbf{k} \times \nabla b, & \text{if } (\mathbf{x}, t) \notin V^J \\ 0, & \text{otherwise} \end{cases}$$

and the viscous part is

$$\mathbf{g}^{WV} = \begin{cases} \nabla \times \mathbf{F}, & \text{if } (\mathbf{x}, t) \notin V^J \\ 0, & \text{otherwise.} \end{cases}$$

The corresponding partial vorticities ζ^{WB} and ζ^{WV} are given in Figs. 3c and 3d, showing that the vertical vorticity of the wake originates primarily in baroclinic generation upstream of the jump. Note that the broad ζ^{WB} anomalies over the lateral slopes of the ridge are suggestive of the baroclinic generation and tilting of vorticity in the mountain wave above the obstacle as described by SR89 and in section 3 of Part I. In the present case the vorticity anomalies extend downstream into the vicinity of the jump where strong amplification occurs to produce the vorticity associated with the shear lines bordering the wake.

The amplification of ζ downstream of the jump is clarified by Figs. 3e and 3f. The vorticity displayed in

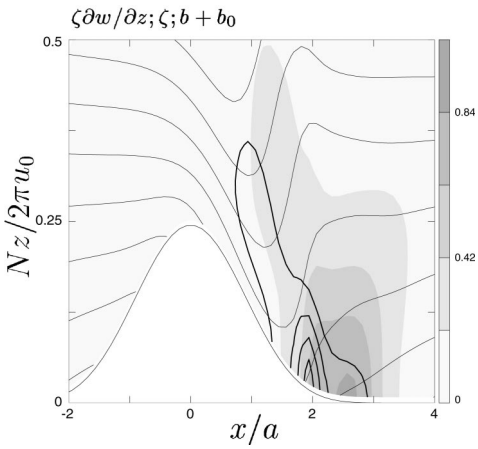

FIG. 4. Vertical vorticity $\zeta/\epsilon^2\delta N$ (shaded contour; contour interval is 0.21) and stretching term $(1/\epsilon^3\delta^2N^2)\zeta\partial w/\partial z$ (heavy line contour; contour interval is 0.16) in cross section through the end of the jump at $y = -2.5a$ at time $u_0t/a = 3$. Thin lines show $(b + b_0)/Nu_0$ (contour interval is 0.5).

Fig. 3e was computed by integrating (26) with the total vorticity source $\mathbf{g}$ but with stretching of vertical vorticity in the jump neglected [i.e., the $\zeta^v\partial w/\partial z$ term in the vertical component of (26a) set to zero for $(\mathbf{x}, t) \in V^J$]. Figure 3f shows a similar calculation but with tilting of horizontal vorticity into the vertical neglected in the jump. Neglecting vertical tilting in the jump has little impact on the vorticity anomalies of the wake, suggesting that tilting in the jump plays a negligible role in producing vertical vorticity. By contrast, neglecting vertical stretching in the jump eliminates the maxima of vertical vorticity downstream of the jump, implying that stretching plays a dominant role in amplifying the vorticity. The spatial distribution of the stretching and the consequent amplification of the vertical vorticity is shown in vertical cross section through the end of the jump (at $y = -2.5a$) in Fig. 4.

Taken together, the results of Figs. 3 and 4 indicate that vorticity generated baroclinically and tilted into the vertical upstream of the jump is amplified by vertical stretching in the jump to produce the pronounced vorticity anomalies associated with the shear lines bordering the wake.

Figure 5 illustrates the roles of viscosity and baroclinicity in generating the cross-stream vorticity η in the centerline plane $y = 0$ (cf. Fig. 2c). The fields shown are the result of decomposing the total vorticity source into baroclinic and viscous parts as

$$\mathbf{g} = \mathbf{g}^B + \mathbf{g}^V,$$

where

$$\mathbf{g}^B = -\mathbf{k} \times \nabla b, \quad \text{and} \quad \mathbf{g}^V = \nabla \times \mathbf{F}.$$

The concentration of η^V near the surface in Fig. 5b reveals the influence of the free-slip lower boundary condition. As implemented in the present simulations the free-slip condition tends to reduce $|\partial u/\partial z|$ and thus $|\eta|$ at the lower boundary. As the flow slowly ascends

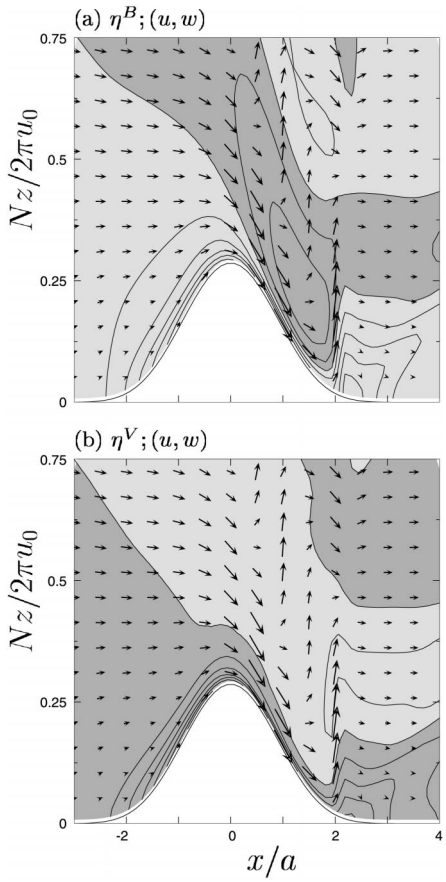

FIG. 5. Decomposition of vorticity according to baroclinic and viscous sources. Fields are shown in the plane of symmetry $y = 0$ at time $u_0t/a = 3$. Vectors in both panels represent the flow field $(u, w)/u_0$: (a, top) baroclinic cross-stream vorticity $\eta^B/\epsilon N$ (contour interval is 0.30); (b, bottom) viscous cross-stream vorticity $\eta^V/\epsilon N$.

the windward slope of the obstacle the negative x-gradient of buoyancy generates strong positive η^B. Viscous effects at the lower boundary oppose the baroclinic generation of η and produce negative η^V to maintain consistency with the free-slip condition. The opposite occurs along the lee slope as the x gradient of buoyancy tends to decrease η while viscous effects act to increase η. However, the flow descends the lee slope rapidly so that both η^B and η^V retain the sense of the vorticity generated on the windward slope. Note that both the wind vectors and the vorticity fields in Figs. 5a,b suggest that the fluid behind the jump has its origins in a very shallow layer of lee-slope flow. As a result of the free-slip condition, the low-level flow entering the jump has only weakly negative net cross-stream vorticity (Fig. 2d). The lack of strong negative η perturbations in the flow entering the jump allows the production of positive η by the cross-jump buoyancy gradient.

5. PV generation and fluxes

Here we consider the role of dissipative processes and PV generation in the viscous $\beta = 3$ and $\epsilon = 1.8$ case described above. To account for the net dissipation in the flow, we extend the definitions of $\mathbf{F}$ and H in section 2b to include the numerical filter terms in (7).

a. Generation of PV in the jump

Downstream of the jump in Fig. 1b, the isentropic surfaces in the flow become relatively level and the horizontal gradients in b are much smaller than upstream of the jump (this is shown for the $\beta = 5$ case in Fig. 4a of ED02). The extension of the vertical vorticity anomalies into this region of nearly level isentropes in Fig. 1b suggests that the potential vorticity Q must be nonzero there as well [cf. (10)]. Figure 6a shows the PV of the wake at time $u_0t/a = 3$; in the lee of the jump the anomalies of PV and vertical vorticity are nearly coincident (compare Figs. 6a and 1b). Note that as with the vertical vorticity, the maxima in PV occur slightly downstream of the lateral edges of the jump, suggesting that the PV of the wake is created primarily in the jump region.

The net PV source in (9) may be divided into a viscous part $\nabla(b + b_0) \cdot (\nabla \times \mathbf{F})$ and a part due to diabatic heating by thermal diffusion $\boldsymbol{\zeta} \cdot \nabla H$. Viscous production of PV results from the direct generation of vorticity with a component normal to the isentropes through the viscous vorticity source $\nabla \times \mathbf{F}$. By contrast, production of PV by thermal diffusion involves modification of the potential temperature field so as to produce PV from the vorticity already present, regardless of the original source of that vorticity. Downstream of the jump (but not upstream) the PV in Fig. 6a is well approximated by $Q \approx \zeta\partial(b + b_0)/\partial z$ (not shown) and is thus mainly associated with the vertical component of $\boldsymbol{\zeta}$. It then follows from the results of section 4 that the vorticity associated with the PV of the wake originates mainly in baroclinic generation upstream of the jump. As such, the production of PV in the jump is expected to be mostly due to thermal diffusion rather than viscous generation. Note in particular that for $H = 0$, any part of the vorticity originating in baroclinic generation (e.g., $\boldsymbol{\zeta}^{WB}$ in Fig. 3) remains everywhere tangent to surfaces of constant $b + b_0$ for all time, regardless of whether $\mathbf{F} = 0$[4]. Thermal diffusion (or more generally, diabatic heating) is thus necessary to produce a component of such vorticity normal to isentropic surfaces.

Figure 6b shows the net PV source dQ/dt [the right-hand side of (9)] on the low-level analysis surface $N\gamma/u_0 \approx \pi/9$. The production of PV is strongest at the lateral edges and somewhat downstream of the jump, with a

[4] This can be proved as follows. Let $\mathbf{g}^\nu$ be equal to $-\mathbf{k} \times \nabla b$ for some specified $(\mathbf{x}, t)$ and zero elsewhere. Taking the dot product of $\nabla(b + b_0)$ with the partial vorticity equation (26a) then yields an equation for $Q^\nu = \boldsymbol{\zeta}^\nu \cdot \nabla(b + b_0)$; that is,

$$\frac{dQ^\nu}{dt} = \boldsymbol{\zeta}^\nu \cdot \nabla H.$$

Since $\boldsymbol{\zeta}^\nu(t_0) = 0$ by definition, $\boldsymbol{\zeta}^\nu \cdot \nabla(b + b_0)$ remains everywhere zero if the flow is adiabatic.

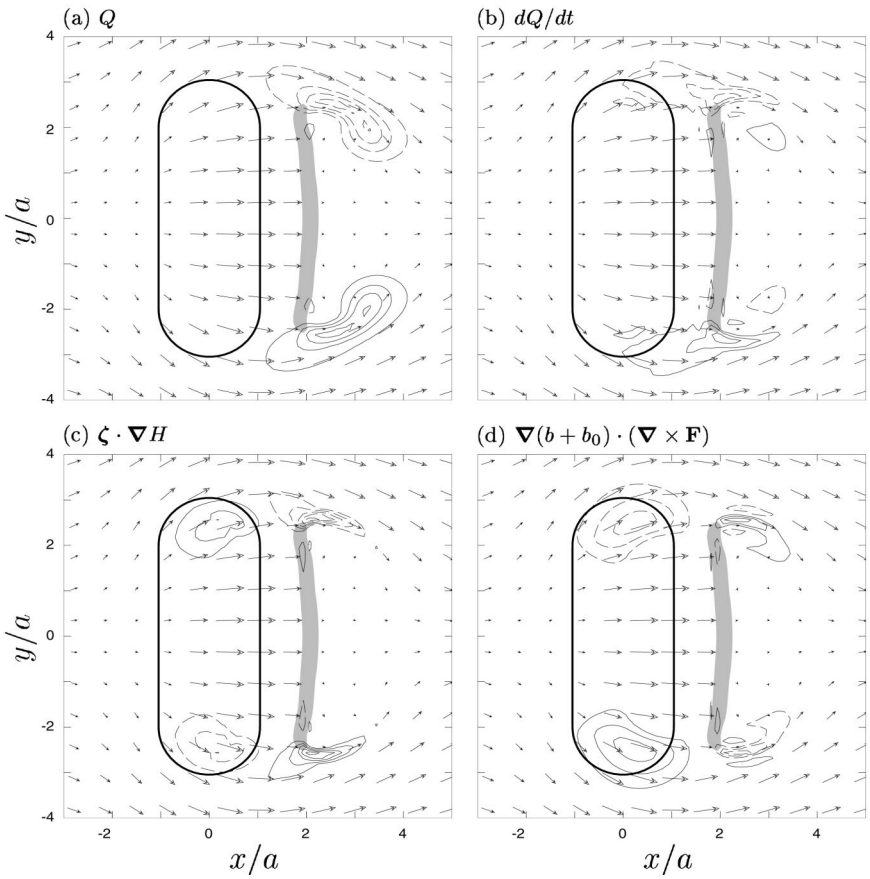

FIG. 6. Potential vorticity Q and material change dQ/dt on low-level analysis surface $N\gamma/u_0 \approx \pi/9$ at time $u_0t/a = 3$. Vectors and shading are as in previous figures: (a) PV $Q/\epsilon^2\delta N^3$ (contour interval is 0.145); (b) total PV source $(1/\epsilon^2\delta^2N^4)dQ/dt$ (contour interval is 0.09); (c) thermal PV source $(1/\epsilon^2\delta^2N^4)\boldsymbol{\zeta} \cdot \boldsymbol{\nabla}H$ (contour interval is 0.09); and (d) viscous PV source $(1/\epsilon^2\delta^2N^4)\boldsymbol{\nabla}(b + b_0) \cdot (\boldsymbol{\nabla} \times \mathbf{F})$ (contour interval is 0.09).

weaker production of PV upstream over the lee slope of the obstacle. The PV source is decomposed into its thermal and viscous parts in Figs. 6c and 6d, showing that the two terms tend to act in opposition to each other. Note that the thermal term dominates the viscous term in the vicinity of the jump and thus determines the sense of the net PV generation in the regions of maximum $|dQ/dt|$. The production of PV in the wake can thus be attributed primarily to the thermal dissipation occurring in the jump region.

Figure 7a shows the net PV source and associated PV in vertical cross section through the end of the jump at $y/a = -2.5$. The generation of PV is concentrated at the base of the jump near $x/a = 2$; the ascending flow in the jump then spreads the PV in the vertical. The thermal and viscous parts of the PV source are shown in Figs. 7b and 7c. The net PV generation is again seen to be dominated by the thermal production of PV in the jump. Further comparison of Figs. 7b and 7d reveals that, in the jump region, the thermal generation of PV is mostly associated with the vertical term $\zeta\partial H/\partial z$. It will be seen in Figs. 9 and 10 that H in the jump is mainly due to the cooling of warm fluid particles crossing the jump near the lower boundary. The resulting $\partial H/\partial z$ is positive and tends to diabatically modify the isentropes so as to increase $\partial(b + b_0)/\partial z$ following the flow. Thermal PV generation then occurs when the vertical vorticity entering the jump from upstream and amplified through stretching is combined with the vertical gradient of diabatic heating in the jump associated with thermal diffusion. Comparison of Figs. 7 and 4 shows that this production of PV by thermal diffusion and the amplification of the vorticity through stretching occur in the same region of the flow.

b. Quasi-steady conservation analysis

Figures 8–10 explore the structure of the wake at time $u_0t/a = 10$ when the flow is roughly steady (or at least slowly varying) in the vicinity of the obstacle. It is then useful to consider the conservation form of the PV equation (11).

As shown by (13), for steady flow the PV flux vector $\mathbf{J}$ is tangent to isentropic surfaces and parallels contours

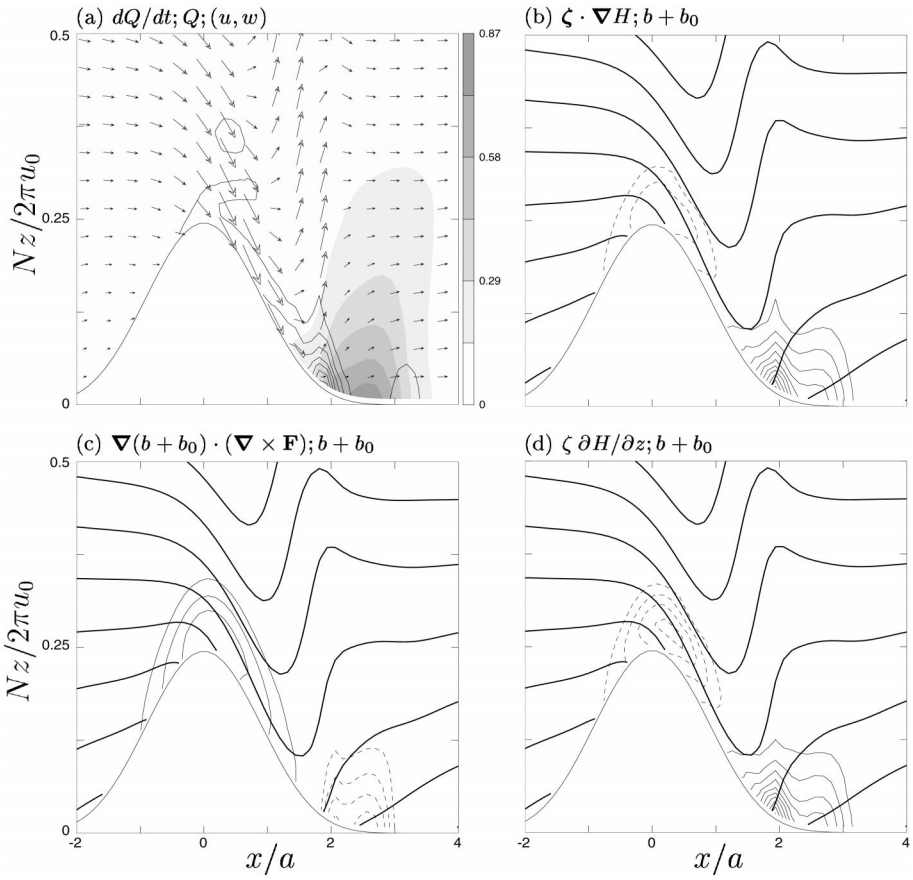

FIG. 7. Potential vorticity generation in vertical cross section through the end of the jump at $y = -2.5a$. Fields are shown at time $u_0 t/a = 3$: (a) total PV source $(1/\epsilon^2\delta^2 N^4)dQ/dt$ (line contour; contour interval is 0.09), potential vorticity $(1/\epsilon^2\delta N^3)Q$ (shaded contour; contour interval is 0.145), and flow field $(u, w)/u_0$; (b) thermal PV source $(1/\epsilon^2\delta^2 N^4)\boldsymbol{\zeta} \cdot \nabla H$ (contour interval is 0.09) and potential temperature $(b + b_0)/Nu_0$ (contour interval is 0.5); (c) viscous PV source $(1/\epsilon^2\delta^2 N^4)\nabla(b + b_0) \cdot (\nabla \times \mathbf{F})$ (contour interval is 0.09); and (d) $(1/\epsilon^2\delta^2 N^4)\zeta\partial H/\partial z$ (contour interval is 0.09).

of the Bernoulli function R on such surfaces. Figure 8 shows $\mathbf{J}$ [as computed from (12)] and R on the isentropic surface with upstream height $z_0/h_0 = 0.62$. The isentrope intersects the topography near the crest of the obstacle and returns to the interior of the flow in the jump. Extending downstream of the ends of the jump are two currents of PV flux, which are associated with advection of Q in the PV streamers at the edges of the wake. The streams of PV flux bound a region of reduced Bernoulli function, reflecting the dissipative history of particles passing over the obstacle and through the jump. As suggested above, the PV fluxes closely parallel contours of R on the surface.

Suppose the flow to be steady and consider the budget for PV fluxes on an isentropic surface such as that shown in Fig. 8. More precisely, consider the PV budget for a thin shell of fluid W bounded above and below by neighboring isentropes like the one in Fig. 8. Let the sides of W be determined by the vertical planes at $y = 0$ and $x = x_2$, where x_2 is downstream of the jump (see dotted lines in Fig. 8). We then have the control volume

$$W = \{(x, y, z) \,|\, -\infty \le x \le x_2,\ -\infty \le y \le 0,\ z \ge h,$$
$$\phi_1 \le b(x, y, z) + b_0(z) \le \phi_1 + \delta\phi\},$$

where ϕ_1 and $\delta\phi$ are constants with $\delta\phi$ taken to be small. We suppose that the intersection of the isentrope $b + b_0 = \phi_1$ with the $x = x_2$ plane is above the obstacle surface for all y but low enough to be in the interior of the wake at $y = 0$ (as for Fig. 8). All disturbance fields are assumed to vanish as $x \to -\infty$ and $y \to -\infty$.

As shown in Fig. 8, there is in general a flux $F_x(x_2)$ of PV out of the volume W at the downstream boundary $x = x_2$. This flux is due to advection of Q in the PV streamers at the edges of the wake and is proportional to the Bernoulli deficit of the wake $\Delta R = R(x_2, -\infty, \phi_1) - R(x_2, 0, \phi_1)$ on the isentrope $b + b_0 = \phi_1$ (see SD97 and S93 for discussion of the relationship between Bernoulli deficit and PV flux). The conservation relation (11) requires that the outward PV flux $F_x(x_2)$ be balanced by an equal inward flux. As discussed above, the flux vector $\mathbf{J}$ is tangent to surfaces of constant $b + b_0$

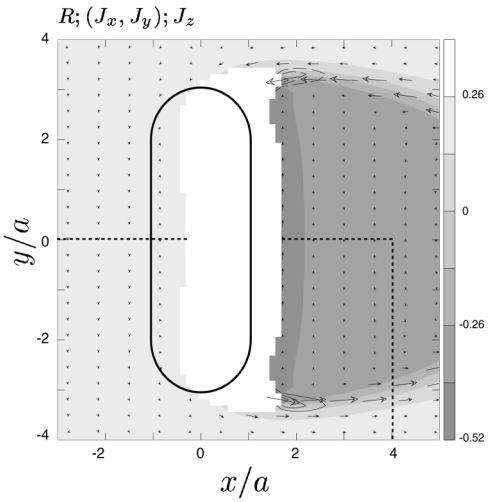

FIG. 8. PV fluxes and Bernoulli function on the isentropic surface with upstream height $z_0/h_0 = 0.62$ ($Nz_0/u_0 = 1.11$) at time $u_0t/a = 10$. Shown are the Bernoulli function $(1/\epsilon u_0^2)R$ (shaded contour; contour interval is 0.13), the horizontal PV flux vectors $(1/\epsilon^2 N^3 u_0 \delta)(J_x, J_y)$ (maximum vector length is 0.4), and the vertical PV flux component $(1/\epsilon^3 N^3 u_0 \delta^2)J_z$ (line contour; contour interval is 0.08). [Bernoulli function in (14) has been shifted by a constant for convenience in labelling.] White area indicates region where isentropic surface intersects lower boundary. Dotted lines show boundaries of control volume W used for analysis of the PV budget.

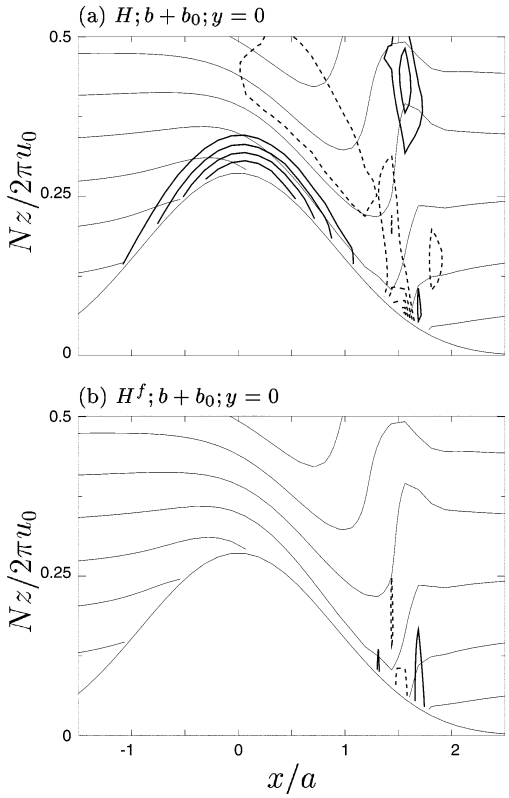

FIG. 9. Diabatic effects in the centerline plane $y = 0$ at time $u_0t/a = 10$: (a) net diabatic heating $(1/\epsilon N^2 u_0 \delta)H$ (heavy lines; contour interval is 0.085) and $(b + b_0)/Nu_0$ (thin solid lines; contour interval is 0.5); (b) as in (a), except for the numerical filter term $(1/\epsilon N^2 u_0 \delta)H^f$. (Note that the horizontal scale has been stretched relative to Figs. 7 and 10 for clarity.)

at steady state so that there is no flux of PV across the isentropic surfaces bounding W (see also Haynes and McIntyre 1987). Two possibilities then exist. If the isentrope $b + b_0 = \phi_1$ nowhere intersects the topography, the outward flux $F_x(x_2)$ must be balanced by a flux $F_y(0) < 0$ across the bounding surface at $y = 0$. If instead the isentrope $b + b_0 = \phi_1$ does intersect the topography, then the boundary of W coincides with the surface of the obstacle over some region S. In this case $F_x(x_2)$ is balanced both by the cross-stream flux $F_y(0)$ and by the flux of PV through S. In all cases the fluxes that balance $F_x(x_2)$ are normal to $\mathbf{u}$ and are thus associated with the dissipative terms in (12).

Figure 1a shows that the isentropic surfaces extending through the region of flow reversal behind the jump all intersect the topography at some point upstream, thus allowing the possibility of PV fluxes through the obstacle surface. Since the flow does not stagnate on the upstream face of the obstacle, the intersection of the isentropes with the topography is necessarily due to diabatic heating by thermal diffusion. Figure 9a shows the net diabatic term H in cross section through the line of symmetry at time $u_0t/a = 10$. The contribution of the numerical filter (7) to H [i.e., $H^f = -\alpha(\partial^4 b/\partial x^4|_\gamma + \partial^4 b/\partial y^4|_\gamma)$] is shown for comparison in Fig. 9b. The diabatic effect of the filter is limited to a weak horizontal heat flux across the jump, thus confirming that the net diabatic heating is dominated by the physical thermal diffusion.[5] Further computation shows that H is well-approximated by the vertical term $K_H \partial^2 b/\partial z^2$ (with $\partial b/\partial z$ set to zero at the lower boundary in accordance with the thermal insulation condition). The phase tilt with height of the wave disturbance over the ridge leads to a downward flux of heat over the crest of the obstacle. This downward heat flux cannot penetrate the thermally insulating lower boundary; as a result, the surface flow is warmed and the isentropes intersect the topography. The opposite occurs at the base of the jump where H is negative and the isentropic surfaces emerge from the topography.

Note that the magnitude of the vertical flux component $|J_z|$ in Fig. 8 is at a maximum at the ends of the jump where the isentrope emerges from the topography. This suggests a flux of PV through the obstacle surface. By contrast, there is no evidence in Fig. 8 of a flux of PV across the centerline $y = 0$. It thus appears that the downstream advection of PV on isentropes passing through the wake is balanced primarily by fluxes of PV through the obstacle surface at the lateral ends of the jump. The PV fluxes through the obstacle surface are shown more clearly in vertical cross section through the end of the jump (at $y = -3.2a$) in Fig. 10. The combination of vertical vorticity amplified through stretch-

[5] Similarly, computing $\boldsymbol{\zeta} \cdot \nabla H^f$ as in Fig. 7b shows that the thermal PV generation associated with the filter is an order of magnitude less than that associated with the physical thermal diffusion.

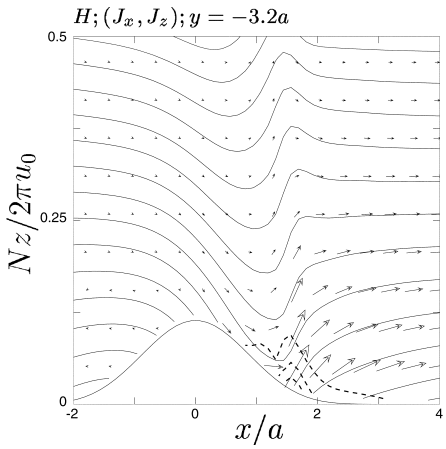

FIG. 10. PV fluxes in vertical cross section through the end of the jump at $y = -3.2a$ at time $u_0t/a = 10$. Shown are the diabatic heating $(1/\epsilon N^2 u_0 \delta)H$ (heavy dashed lines; contour interval is 0.085) and potential vorticity flux $(1/\epsilon^2 N^3 u_0 \delta)(J_x, J_z)$. Thin lines show $(b + b_0)/Nu_0$ (contour interval is 0.25).

ing and diabatic cooling at the base of the jump produces a vertical component $J_z \approx -\zeta H > 0$ at the lower boundary, resulting in a net flux of PV through the topography.

According to (11), PV fluxes in the interior of a fluid necessarily produce equal amounts of positive and negative PV. By contrast, fluxes of PV through the lower boundary provide a mechanism for generating asymmetric PV anomalies. Orographic wakes with unequal amounts of positive and negative PV are likely to be observed in flows with asymmetric topography, asymmetric basic states, and/or background rotation.

6. Summary and discussion

This study has explored mechanisms of vorticity and PV production in viscous stratified flow over ridges with free-slip surfaces. Particular emphasis has been given to fully nonlinear effects and to the role of the hydraulic jump in producing vorticity and PV.

A diagnostic method involving Lagrangian decompositions of the vorticity field was developed based on a propagator analysis of the Lagrangian vorticity equation. The method was then applied to the nonlinear viscous simulations to clarify mechanisms of vorticity production. The vertical vorticity at the lateral edges of the wake is found to have its origins in baroclinic generation and tilting in the mountain wave upstream of the jump, as originally suggested by SR89. However, upstream of the jump the vertical vorticity is relatively weak. *Upon reaching the jump the vorticity is amplified several-fold through stretching to produce the pronounced vertical vorticity anomalies along the wake shearlines.* In vertical cross section, viscous effects near the free-slip lower boundary inhibit the baroclinic generation of negative cross-stream vorticity $\eta \approx \partial u/\partial z$ at low levels along the lee slope. (Note that a surface friction condition would locally act in the same sense.) Upon crossing the jump the low-level flow deepens, decelerates, and gains positive η due to the buoyancy gradient across the jump. The negative $u - u_0$ and positive $\partial u/\partial z$ downstream of the jump are then consistent with reversal of the surface flow.

In the viscous laminar model the vertical vorticity anomalies along the shearlines downstream of the jump are nearly coincident with anomalies in PV, suggesting that PV is produced in the jump. The generation of PV in the jump occurs primarily through thermal diffusion tending to modify the potential temperature field following the flow so as to produce PV from the vertical vorticity already present in the jump. This thermal PV generation occurs in the same region of the flow as the amplification of the vertical vorticity through stretching. From the perspective of PV conservation, diabatic cooling at the base of the jump produces a vertical com-

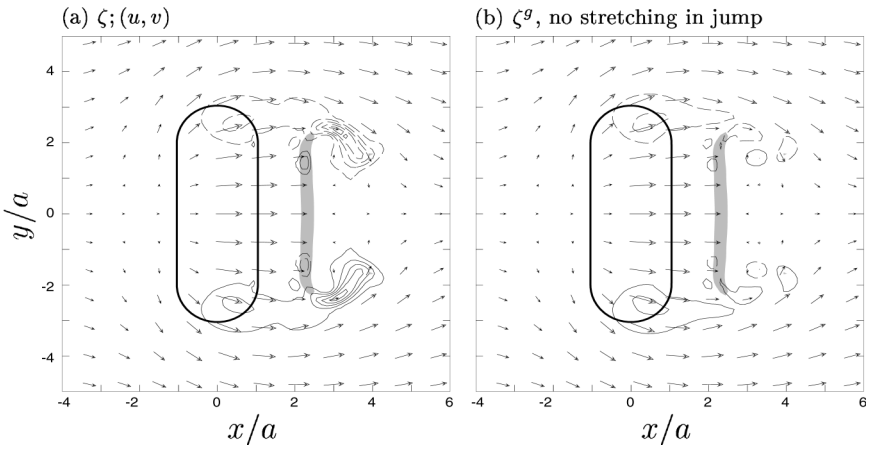

FIG. 11. Basic wake features in the $\epsilon = 1.8$, $\beta = 3$ case with viscosity determined through subgrid-scale turbulence parameterization. Contour intervals and vector lengths are as in previous figures except that shading indicates values of $(a/\epsilon N u_0)\partial b/\partial x$ less than -0.65: (a) vertical vorticity $\zeta/\epsilon^2 \delta N$ and horizontal velocity $(u, v)/u_0$ as in Fig. 1b; (b) vorticity computation with stretching of vertical vorticity neglected in the jump as in Fig. 3e.

ponent of PV flux $J_z \approx -\zeta H$ at the lower boundary resulting in a net flux of PV through the obstacle surface. As a result, the downstream advection of PV on either side of the wake is primarily balanced at steady state by fluxes of PV through the obstacle surface.

It remains to be seen how well the mechanisms of wake formation in the viscous laminar model extend to more realistic flows with surface friction and turbulence. Nominally inviscid simulations in which the viscosity represents the effects of small-scale turbulence provide some indication that the basic features of the viscous model extend also to free-slip turbulent flows. Figure 11 shows results of a numerical simulation of the $\epsilon = 1.8$, $\beta = 3$ case considered previously but with the viscosity specified through the subgrid-scale turbulence parameterization of Lilly (1962). Comparison of Fig. 11a with Fig. 1b shows that the wake is similar in structure to that obtained in the viscous case. Preliminary analysis suggests that the detailed mechanisms of vorticity generation upstream of the jump in the eddy-viscosity case may be somewhat different than in the viscous laminar model. Nonetheless, Fig. 11b shows that stretching in the jump again plays a dominant role in amplifying the vertical vorticity. It is currently unclear whether the subgrid-scale turbulence parameterization provides an adequate description of the averaged properties of real turbulent flows. As such, we postpone further discussion of this case for future work.

Acknowledgments. The authors are indebted to Dave Muraki for suggesting a propagator interpretation for (22) (which was originally derived by other means). We also gratefully acknowledge helpful discussions with Rich Rotunno; Vanda Grubišić provided useful comments on a draft of this work. This research was sponsored by NSF Grants ATM-9530662 and ATM-9817728. Part of this work was completed while C.C. Epifanio was the recipient of a postdoctoral fellowship in the Advanced Study Program at the National Center for Atmospheric Research (NCAR). NCAR is sponsored by NSF.

APPENDIX A

Derivation of the Vorticity Propagator

The Lagrangian expression for the vorticity propagator (20) can be derived as follows. Integrating (17a) across the impulsive forcing at $t = \tau$, we find that the propagator $\mathbf{P}$ is determined for $t > \tau$ by the equivalent initial-value problem,

$$\frac{dP_{ij}}{dt}(t, \tau) = M_{ik}(t)P_{kj}(t, \tau), \qquad P_{ij}(\tau^+, \tau) = \delta_{ij}, \quad \text{(A1)}$$

where the initial condition is formally applied for $t \to \tau^+$. To solve (A1), we first consider the initial-value problem with initial condition at t_0; that is,

$$\frac{d\Phi_{ij}}{dt}(t) = M_{ik}(t)\Phi_{kj}(t) = \frac{\partial u_i}{\partial x_k}(t)\Phi_{kj}(t), \quad \text{and} \quad \text{(A2a)}$$

$$\Phi_{ij}(t_0) = \delta_{ij}. \quad \text{(A2b)}$$

Note that by definition, $\mathbf{\Phi}$ is a fundamental matrix solution of the linear system (16) (e.g., Coddington and Levinson 1955). With the notation defined in (19), we next rewrite (A2a) in the form

$$\frac{\partial \Phi_{ij}}{\partial t_X} = \frac{\partial u_i}{\partial X_r}\frac{\partial X_r}{\partial x_k}\Phi_{kj} = \frac{\partial}{\partial t_X}\left(\frac{\partial x_i}{\partial X_r}\right)\frac{\partial X_r}{\partial x_k}\Phi_{kj}, \quad \text{(A3)}$$

where we have used the definition $u_i = \partial x_i/\partial t_X$. The solution to (A3) with (A2b) is then seen to be the Jacobian matrix

$$\Phi_{ij} = \frac{\partial x_i}{\partial X_j}, \quad \text{(A4)}$$

since $(\partial X_r/\partial x_k)\,(\partial x_k/\partial X_j) = \delta_{rj}$ and $\partial x_i/\partial X_j(t_0) = \delta_{ij}$.

Given $\mathbf{\Phi}(t)$, a solution to (A1) can be formed as

$$P_{ij}(t, \tau) = \Phi_{ik}(t)\Phi^{-1}_{kj}(\tau), \quad \text{(A5)}$$

as is verified by noting that $P_{ij}(\tau^+, \tau) = \Phi_{ik}(\tau)\Phi^{-1}_{kj}(\tau) = \delta_{ij}$ and

$$\frac{dP_{ij}}{dt}(t, \tau) = M_{ir}(t)\Phi_{rk}(t)\Phi^{-1}_{kj}(\tau) = M_{ik}(t)P_{kj}(t, \tau), \quad \text{(A6)}$$

where the first equality follows from (A2a) and the second from (A5) after exchanging summation indices k and r. Since $(\partial x_i/\partial X_k)\,(\partial X_k/\partial x_j) = \delta_{ij}$, the inverse matrix is

$$\Phi^{-1}_{ij} = \frac{\partial X_i}{\partial x_j}. \quad \text{(A7)}$$

Substituting (A4) and (A7) into (A5) we obtain the propagator (20).

APPENDIX B

Numerical Implementation of Vorticity Integrations

The numerical model described in section 2 of Part I employs a C grid in which the discretized velocity fields u_i are staggered from the thermodynamic fields (i.e., P and b) by a distance of $\Delta x_i/2$ in the ith coordinate direction. Leapfrog time differencing is used on the large time step Δt and forward–backward differencing on the small time step Δt_s (see Durran 1999, section 7.3). In integrating (26a) the partial vorticity variables $\boldsymbol{\zeta}^\nu$ are defined at the thermodynamic grid points and the integrations are computed entirely on the large time step.

We first rewrite (26a) as

$$\frac{\partial \xi^\nu}{\partial t} = \xi^\nu \frac{\partial u}{\partial x} + \eta^\nu \frac{\partial u}{\partial y} + \zeta^\nu \frac{\partial u}{\partial z} + f_\xi, \tag{B1}$$

$$\frac{\partial \eta^\nu}{\partial t} = \xi^\nu \frac{\partial v}{\partial x} + \eta^\nu \frac{\partial v}{\partial y} + \zeta^\nu \frac{\partial v}{\partial z} + f_\eta, \quad \text{and} \tag{B2}$$

$$\frac{\partial \zeta^\nu}{\partial t} = \xi^\nu \frac{\partial w}{\partial x} + \eta^\nu \frac{\partial w}{\partial y} + \zeta^\nu \frac{\partial w}{\partial z} + f_\zeta, \tag{B3}$$

where $\mathbf{f} = (f_\xi, f_\eta, f_\zeta)$ is given by

$$\mathbf{f} = -(\mathbf{u} \cdot \nabla)\boldsymbol{\zeta}^\nu + \mathbf{g}^\nu. \tag{B4}$$

Note that if $\mathbf{f} = 0$ and the velocity gradients are taken as constants, Eqs. (B1)–(B3) have solutions that exponentially grow or decay in time. A simple single-equation constant-coefficient stability analysis of an exponential growth–decay equation shows leapfrog time differencing of the equation to be numerically unstable. To avoid the possible instability associated with leapfrog differencing in growth-decay problems, we compute the stretching and tilting terms in (B1)–(B3) with implicit time differences. Equations (B1)–(B3) are then discretized as (dropping the superscript ν for convenience)

$$\delta_{2t}\xi = \langle \xi \rangle^{2t} \frac{\partial u^t}{\partial x} + \langle \eta \rangle^{2t} \frac{\partial u^t}{\partial y} + \langle \zeta \rangle^{2t} \frac{\partial u^t}{\partial z} + f_\xi^t, \tag{B5}$$

$$\delta_{2t}\eta = \langle \xi \rangle^{2t} \frac{\partial v^t}{\partial x} + \langle \eta \rangle^{2t} \frac{\partial v^t}{\partial y} + \langle \zeta \rangle^{2t} \frac{\partial v^t}{\partial z} + f_\eta^t, \tag{B6}$$

and

$$\delta_{2t}\zeta = \langle \xi \rangle^{2t} \frac{\partial w^t}{\partial x} + \langle \eta \rangle^{2t} \frac{\partial w^t}{\partial y} + \langle \zeta \rangle^{2t} \frac{\partial w^t}{\partial z} + f_\zeta^t, \tag{B7}$$

where the superscript t indicates the middle time level and where the time differencing and averaging operators are defined as

$$\delta_{2t}\phi = \frac{\phi^{t+\Delta t} - \phi^{t-\Delta t}}{2\Delta t}, \quad \text{and} \quad \langle \phi \rangle^{2t} = \frac{1}{2}(\phi^{t+\Delta t} + \phi^{t-\Delta t}).$$

The horizontal spatial derivatives in (B5)–(B7) and (B4) are computed using fourth-order centered differences, and second-order centered differences are used for the vertical derivatives.

Equations (B5)–(B7) yield the matrix equation,

$$\Delta t \begin{pmatrix} \frac{\partial u}{\partial x} - \frac{1}{\Delta t} & \frac{\partial u}{\partial y} & \frac{\partial u}{\partial z} \\ \frac{\partial v}{\partial x} & \frac{\partial v}{\partial y} - \frac{1}{\Delta t} & \frac{\partial v}{\partial z} \\ \frac{\partial w}{\partial x} & \frac{\partial w}{\partial y} & \frac{\partial w}{\partial z} - \frac{1}{\Delta t} \end{pmatrix}^t \begin{pmatrix} \xi \\ \eta \\ \zeta \end{pmatrix}^{t+\Delta t} = -\begin{pmatrix} \xi_e \\ \eta_e \\ \zeta_e \end{pmatrix}, \tag{B8}$$

where

$$\begin{pmatrix} \xi_e \\ \eta_e \\ \zeta_e \end{pmatrix} = \Delta t \begin{pmatrix} \frac{\partial u}{\partial x} + \frac{1}{\Delta t} & \frac{\partial u}{\partial y} & \frac{\partial u}{\partial z} \\ \frac{\partial v}{\partial x} & \frac{\partial v}{\partial y} + \frac{1}{\Delta t} & \frac{\partial v}{\partial z} \\ \frac{\partial w}{\partial x} & \frac{\partial w}{\partial y} & \frac{\partial w}{\partial z} + \frac{1}{\Delta t} \end{pmatrix}^t \begin{pmatrix} \xi \\ \eta \\ \zeta \end{pmatrix}^{t-\Delta t} + 2\Delta t \begin{pmatrix} f_\xi \\ f_\eta \\ f_\zeta \end{pmatrix}^t. \tag{B9}$$

The matrix in (B8) is inverted analytically using Cramer's rule to give $(\xi, \eta, \zeta)^{t+\Delta t}$ in terms of variables at time levels t and $t - \Delta t$.

REFERENCES

Coddington, E. A., and N. Levinson, 1955: *Theory of Ordinary Differential Equations.* McGraw-Hill, 428 pp.

Durran, D. R., 1999: *Numerical Methods for Wave Equations in Geophysical Fluid Dynamics.* Springer-Verlag, 460 pp.

Dutton, J. A., 1976: *The Ceaseless Wind.* McGraw-Hill, 579 pp.

Epifanio, C. C., and D. R. Durran, 2002: Lee-vortex formation in free-slip stratified flow over ridges. Part I: Comparison of weakly nonlinear inviscid theory and fully nonlinear viscous simulations. *J. Atmos. Sci.,* **59,** 1153–1165.

Grimshaw, R., 1993: *Nonlinear Ordinary Differential Equations.* CRC Press, 336 pp.

Haynes, P. H., and M. E. McIntyre, 1987: On the evolution of vorticity and potential vorticity in the presence of diabatic heating and frictional or other forces. *J. Atmos. Sci.,* **44,** 828–841.

Lilly, D. K., 1962: On the numerical simulation of buoyant convection. *Tellus,* **14,** 148–172.

Morton, B. R., 1984: The generation and decay of vorticity. *Geophys. Astrophys. Fluid Dyn.,* **28,** 277–308.

Pratt, L. J., 1983: On inertial flow over topography. Part I. Semi-geostrophic adjustment to an obstacle. *J. Fluid Mech.,* **131,** 195–218.

Rotunno, R., and P. K. Smolarkiewicz, 1991: Further results on lee vortices in low-Froude-number flow. *J. Atmos. Sci.,* **48,** 2204–2211.

——, V. Grubišić, and P. K. Smolarkiewicz, 1999: Vorticity and potential vorticity in mountain wakes. *J. Atmos. Sci.,* **56,** 2796–2810.

Schär, C., 1993: A generalization of Bernoulli's theorem. *J. Atmos. Sci.,* **50,** 1437–1443.

——, and R. B. Smith, 1993: Shallow-water flow past isolated topography. Part I: Vorticity production and wake formation. *J. Atmos. Sci.,* **50,** 1373–1400.

——, and D. R. Durran, 1997: Vortex formation and vortex shedding in continously stratified flows past isolated topography. *J. Atmos. Sci.,* **54,** 534–554.

Serrin, J., 1959: Mathematical principles of classical fluid mechanics. *Handbuch der Physik,* S. Flügge, Ed., Vol. VIII. Springer-Verlag, 125–163.

Smith, R. B., 1980: Linear theory of stratified hydrostatic flow past an isolated mountain. *Tellus,* **32,** 348–364.

Smolarkiewicz, P. K., and R. Rotunno, 1989: Low Froude number flow past three-dimensional obstacles. Part I: Baroclinically generated lee vortices. *J. Atmos. Sci.,* **46,** 1154–1164.